Research Paper

Petrogenesis of granitic pegmatite veins: Perspectives from major element and B isotope in tourmalines, Chakabeishan, Northern Tibetan Plateau

Wenli Sun [a,b,c], Zhidan Zhao [a,*], Yaoling Niu [a,d], Chunjing Wei [b], Guochen Dong [a], Xiaowei Li [a], Wanming Yuan [a], Tao Wang [e], Bingzhang Wang [e], Tong Pan [e], Jie Han [e], Hongliang Cao [e], Yan Tang [a], Dicheng Zhu [a]

[a] *State Key Laboratory of Geological Processes and Mineral Resources, and School of Earth Science and Resources, China University of Geosciences, Beijing 100083, China*
[b] *MOE Key Laboratory of Orogenic Belts and Crustal Evolution,School of Earth and Space Sciences, Peking University, Beijing 100871, China*
[c] *Gansu Industry Polytechnic College, Tianshui 741025, China*
[d] *Laoshan Laboratory, Qingdao 266237, China*
[e] *Bureau of Geological Exploration and Development of Qinghai Province, Xining 810012, China*

A R T I C L E   I N F O

A B S T R A C T

The petrogenesis of regionally zoned granitic pegmatite veins remains debated. Because of the economic significance, we carried out a study on the Chakabeishan (CKBS) pegmatite-type Li-Be deposit, eastern North Qaidam Tectonic Belt, Northern Tibetan Plateau, by means of in-situ major element and B isotope compositions of tourmalines in the beryl-bearing and spodumene-bearing pegmatite veins. Tourmalines (Tur-Be) from the beryl-bearing pegmatite are homogeneous schorl with low Mg/(Mg + Fe), high Na/(Na + Ca) and ^{Y}Al, suggesting that they are of magmatic origin. Two generations of tourmalines (Tur-Li) from the spodumene-bearing pegmatite are identified: (i) the crystal cores (mostly elbaite and Li-rich schorl with subordinate schorl) are consistent with being of magmatic origin crystallized at the magmatic stage; (ii) the crystal rims (schorl) are best understood as the overgrowth at the later hydrothermal stage. Tur-Be and Tur-Li show an obvious difference in core-to-rim B isotopic variation trend with δ^{11}B decrease in Tur-Be and increase in Tur-Li. The core-to-rim δ^{11}B decrease in Tur-Be results from degassing during its host pegmatitic melt evolution, whereas the core-to-rim δ^{11}B increase in Tur-Li is related to fluid exsolution. The estimated δ^{11}B values for the initial melts of the beryl-bearing and spodumene-bearing pegmatites are −10.46‰ and −10.78‰, respectively, indicating that they most likely originate from protracted fractional crystallization/differentiation of granitic intrusions rather than partial melting of metapelite. Both Mg/(Mg + Fe) ratios and Li abundances in the cores of Tur-Be are lower than those of Tur-Li, suggesting that Tur-Li crystallizes from chemically more evolved melts.

1. Introduction

Granitic pegmatite (hereafter pegmatite) is a typical product of magmatic-hydrothermal system evolution, and is one of the major hosts for rare metals, gemstones and industrial materials (e.g., Chen et al., 2020; London, 2018; Sun et al., 2021; Thomas and Davidson, 2015; Trumbull et al., 2013; Troch et al., 2022). Because of the economic significance, pegmatites have been the focus of much recent discussion, yet their petrogenesis and mineralization remain debated (e.g., Jahns and Burnham, 1969; London, 2015;

Thomas and Davidson, 2015). Pegmatites have a granitic composition with high fluxing components (e.g., H_2O, F, B, P and alkalis), and tend to be systematically distributed within and/or around coeval granites. They are thus generally considered to have resulted from protracted fractional crystallization of granitic magmas, in which rare metals as incompatible elements accumulate in the residual melts (e.g., Jahns and Burnham, 1969; Černý, 1991; Hulsbosch et al., 2014; London, 2018). However, such connections between pegmatites and adjacent granites cannot always be established (e.g., Chen et al., 2020; Zhao et al., 2022). In fact, it is commonplace to observe isolated pegmatites that lack exposures of parental granitic intrusions. The isolated pegmatites have been theoretically connected to "deeply buried granite" because peg-

matitic melts can and do migrate up to kilometers from parental granitic magma (Baker, 1998; London, 2018). However, an alternative interpretation for the origin of isolated pegmatites has been source-rock partial melting, i.e., pegmatite-forming melt is directly generated by low degree melting of *meta*-sedimentary rocks under amphibolite or granulite facies conditions at mid-crustal levels (e.g., Chen et al., 2020; Lv et al., 2021). The partial melting model suggests that the enrichments of rare metals in pegmatites are mainly controlled by the partial melting mechanism and the chemical composition of the source rocks (e.g., Chen et al., 2020; Lv et al., 2021; Zhao et al., 2022).

The principal difficulty on the petrogenesis of pegmatite lies in the fact that the composition of melt parental to the pegmatite cannot be reasonably obtained due to its complex internal zonation, huge crystal size, ubiquitous and varied post-magmatic alteration (e.g., London, 2018; Wise and Brown, 2019), i.e., the bulk-rock composition approach for the petrogenesis of other magmatic rocks does not apply to the petrogenesis of pegmatite. Hence, an alternative approach is needed to trace the geochemical evolution of pegmatite-forming melt by tracking compositional changes for a specific mineral that forms and develops throughout the evolution history (e.g., Slack and Trumbull, 2011; Hulsbosch et al., 2014; Xing et al., 2020; Yan et al., 2022). Some minerals are better suited for this purpose than others, but tourmaline is one of the best because tourmaline is a ubiquitous accessory phase that can form in both silicate magmas and hydrothermal fluids (e.g., da Costaet al., 2014; Drivenes et al., 2015; Cheng et al., 2021; Zhao et al., 2021), and can be stable over a wide range of pressures, temperatures and fluid compositions once formed (van Hinsberg et al., 2011). Meanwhile, tourmaline has a crystal structure of $XY_3Z_6T_6O_{18}(BO_3)_3V_3W$ that is capable of accommodating a variety of major and trace elements with slow diffusion rates (Henry et al., 2011; van Hinsberg et al., 2011), and can thus record valuable information on the nature of the melts/fluids from which it formed and hence can be used to trace the magmatic-hydrothermal processes (e.g., Jiang and Palmer, 1998; Slack and Trumbull, 2011; van Hinsberg et al., 2011; Drivenes et al., 2015; Bosi, 2018; Cheng et al., 2021; Zhao et al., 2021).

The Chakabeishan (CKBS) deposit is the first pegmatite-type Li-Be deposit discovered in the eastern North Qaidam Tectonic Belt (NQTB), Northern Tibetan Plateau (Pan et al., 2021; Sun et al., 2023; Fig. 1a). Since its discovery in 2018, geochronology, bulk-rock geochemistry, Hf-Nd isotope and muscovite-feldspar-garnet mineralogy of the pegmatite veins in the CKBS deposit have been documented (e.g., Wang et al., 2020a; Wang et al., 2020b; Pan et al., 2021; Chen et al., 2022; Liu et al., 2022a; Liu et al., 2022b; Liu et al., 2023; Sun et al., 2023). Based on these data, the petrogenesis of pegmatites in the CKBS deposit has been discussed, yet the issue is still controversial (e.g., Liu et al., 2022a; Liu et al., 2022b; Liu et al., 2023). Here, this study focuses on in-situ major element and boron isotope analysis on the tourmalines in the beryl- and spodumene-bearing pegmatite veins from the CKBS deposit with the aim of revealing the evolution history of the melts parental to the pegmatites, tracing the origin of the pegmatite-forming melts and deciphering the B isotope fractionation in the Li-rich and Be-rich pegmatites.

2. Geological backgrounds

2.1. Regional geology

The NQTB is located between the Qaidam Block to the south and the Qilian Block to the north, southeast of the Altyn Tagh fault, and merges with the West Qinling orogenic belt to the east (Fig. 1b; Wu et al., 2014; Li et al., 2018). It is divided into southern and northern

tectonic units by the Yuka-Wulan fault (Fig. 1b). The southern unit is an Early Paleozoic subduction-collision complex related to Proto-Tethys seafloor subduction, consisting of Tianjianshan volcanic zone and ultra-high pressure (UHP) metamorphic belt (e.g., Song et al., 2014; Wu et al., 2014). The Tianjianshan volcanic zone was developed due to northward seafloor subduction during 540–500 Ma (Pan et al., 2021). The UHP metamorphic belt is a typical Alpine-type UHP metamorphic belt and resulted from the continental collision of the Qaidam Block with the Qilian Block. The UHP metamorphic belt is dominated by orthogneisses and paragneisses with minor blocks of eclogite, mafic granulite, amphibolites, marble and garnet peridotite (Song et al., 2014; Yu et al., 2019; Ren et al., 2021). The northern unit is also called Quanji Massif, which is characterized by components of a double-layered structure (Zhang et al., 2014; Li et al., 2018; Ren et al., 2021). Its metamorphic basement includes the Paleoproterozoic Delingha complex, Dakendaban Group and Mesoproterozoic Wandonggou Group (e.g., Chen et al., 2012; Zhang et al., 2014; Li et al., 2018; Wang et al., 2020a; Wang et al., 2020b). The basement of the Quanji Massif is uncomfortably overlain by the Nanhua-Sinian Quanji Group and Paleozoic – Mesozoic strata (Zhang et al., 2014; Li et al., 2018).

2.2. Geology of the CKBS deposit

The CKBS pegmatite-type Li-Be deposit is located in the eastern NQTB, in which pegmatite veins occur as veins and lenses (Liu et al., 2023). Coltan U-Pb dating reveals that the formation age of these pegmatite veins is ~ 240 Ma (Pan et al., 2021). The elongation of these pegmatite veins varies (Fig. 1c), but generally shows NW−SE trending with varying dipping (23°−83°). The pegmatite veins are mostly 10–400 m in length and 0.5–5 m in width. They consist of coarse-grained to pegmatitic quartz + plagioclase + K-feldspar+tourmaline±garnet±muscovite±spodumene±beryl±apatite ± coltan (Wang et al., 2020a; Liu et al., 2023). Unlike Koktokay No.3 vein (Sun et al., 2021) and Wellington Lake pegmatite veins (Raschke et al., 2021), the CKBS pegmatite veins lack evident internal structural and mineralogical zonation (Supplementary Data Fig. S1a). On the contrary, they display regional zonation in terms of the dominant rare-metal mineralization and wall rock lithology (Fig. 1c), as documented in pegmatites of the Jiajika, Zhawulong and Gatumba areas (e.g., Hulsbosch et al., 2014; Li et al., 2015; Yan et al., 2020; Sun et al., 2021). The zone-I is characterized by Li-rich and Li-Be-rich pegmatite veins hosted in the Ordovician quartz diorite. The contact between the pegmatite veins and the host quartz diorite is irregular but sharp without alteration (Supplementary Data Fig. S1b). Seventeen ore bodies have been discovered in the zone-I with an average Li_2O grade of 0.9–2.15 wt.% and BeO grade of 0.04–0.08 wt.% (Liu et al., 2021). The elongation of these bodies is chaotic, but generally is 290°−320° with different dipping (20°−50°). They are mostly 80–340 m in length and of 0.5–5 m in width (Liu et al., 2022a). The zone-II in the CKBS deposit is marked by Be-rich pegmatite veins hosted in schist with the pegmatite-schist contact being sharp and showing tourmaline and apatite alteration in places (Supplementary Data Fig. S1c). Fifty-three ore bodies have been found in the zone-II, showing BeO abundances of 0.04–0.11 wt.%. Their striking and dipping are similar to those of the seventeen ore bodies in the zone-I. They are mostly 50–660 m in length and 0.3–6.5 m in width (Liu et al., 2022b). The pegmatites in the zone-III are emplaced in the mylonitic Ordovician quartz diorite (Supplementary Data Fig. S1d). Although a few pegmatite veins show Be-rich information, *ca.* 93 % pegmatite veins in the zone-III are barren pegmatites and most of the pegmatite veins are tourmaline pegmatite, muscovite garnet tourmaline pegmatite and graphic pegmatite.
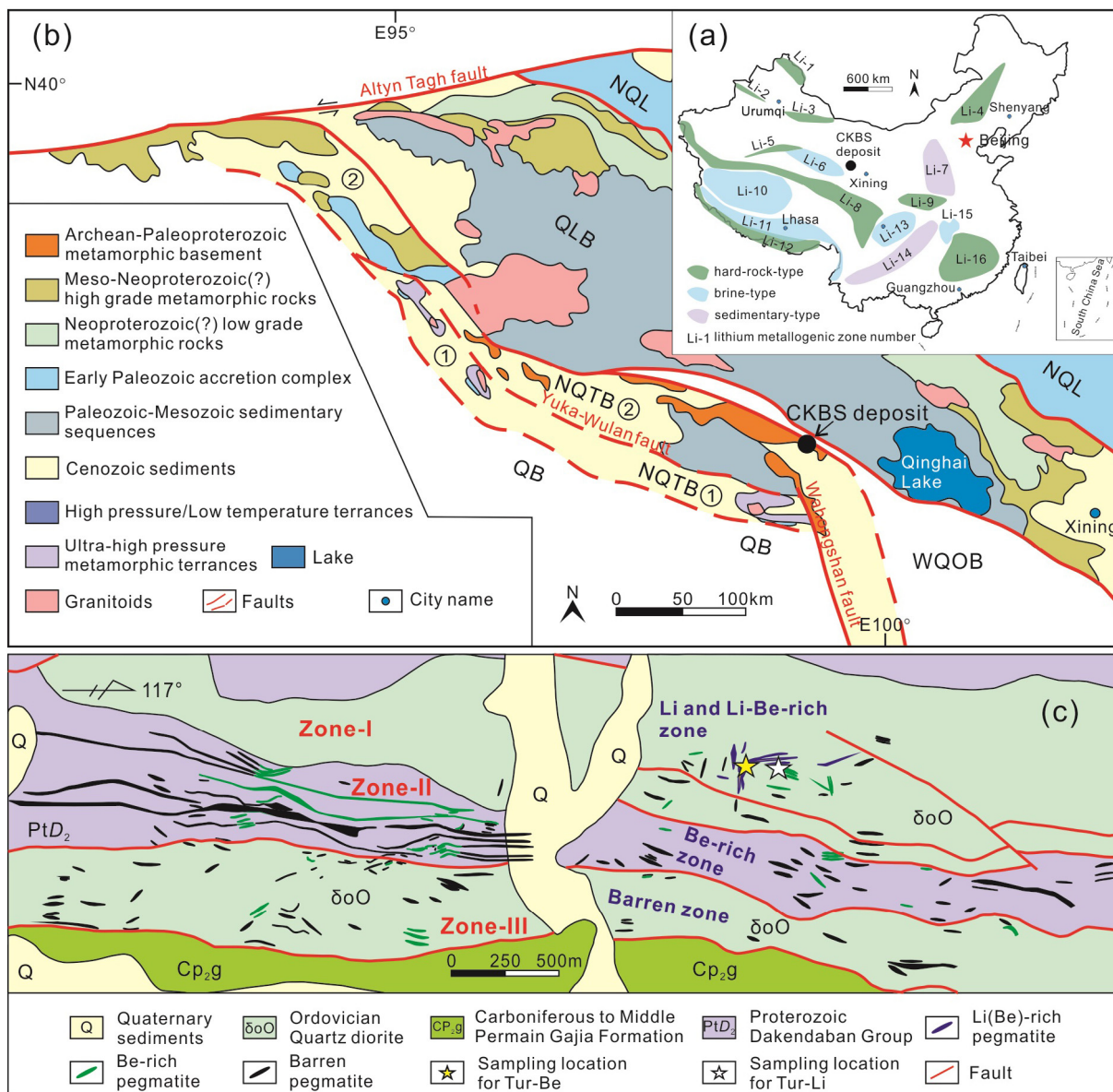
Fig. 1. (a) Sketch map showing the Li metallogenic belts in China and the location of the CKBS deposit (modified after Zhang et al., 2022). Li-1 to Li-16 are important Li metallogenic belts in China (Zhang et al., 2022). (b) Geological sketch of the NQTB and its surrounding tectonic units (modified after Chen et al., 2012; Li et al., 2018; Pan et al., 2021; Ren et al., 2021). ①-Southern tectonic unit of the NQTB; ②-Northern tectonic unit of the NQTB; NQTB-North Qaidam Tectonic Belt; QB-Qaidam Block; NQL-North Qilian subduction accretionary complex; QLB-Qilian Block; WQOB-Western Qinling Orogenic Belt. (c) Geological sketch showing the regionally zoned pegmatite veins in the CKBS Li-Be deposit.

3. Samples and analytical methods

3.1. Samples

In this study, double polished thin sections were made for beryl-bearing and spodumene-bearing pegmatite samples (Table 1) for petrography and for major element and boron isotope analysis

of tourmalines. Tourmalines (Tur-Be) from the beryl-bearing pegmatite veins occur as subhedral to euhedral crystals (Fig. 2a–c). In plane-polarized light, Tur-Be shows uniform optical properties with dark-to-light blue pleochroism and contains a large number of mineral inclusions of varying size (Fig. 2b, c). Tourmalines (Tur-Li) from the spodumene-bearing pegmatite veins occur mainly as anhedral crystals and a few as subhedral (Fig. 2d–i). In

Table 1
Summary of pegmatite samples of this study.

Sample #	Rock type	Pegmatite #	Location		Mineralogy (+accessory phases)
CK2003-4	spodumene-bearing pegmatite	ρ15	37°01′26″N	99°03′22″E	Q 25%, Ab 25%, Kfs 8%, Sp 28%, Tur 10% (Mus, Zrn, Ap)
CK2007-2	spodumene-bearing pegmatite	ρ15	37°01′25″N	99°03′22″E	Q 30%, Ab 28%, Kfs 10%, Sp 20%, Tur 8%, Mus 3% (Zrn, Grt, Ap)
CK2008-4	beryl-bearing pegmatite	ρ19	37°01′23″N	99°03′25″E	Q 23%, Ab 25%, Kfs 35%, Tur 10 %, Mus 5% (Byl, Grt Zrn, Ap)
CK2008-6	beryl-bearing pegmatite	ρ19	37°01′23″N	99°03′25″E	Q 20%, Ab 30%, Kfs 35%, Tur 8%, Mus 5% (Byl, Grt Zrn, Ap)

Q-quartz; Ab-ablite; Kfs-K-feldspar; Sp-spodumene; Tur-tourmaline; Mus-muscovite; Byl-beryl; Zrn-zircon; Ap-apatite; Grt-garnet.
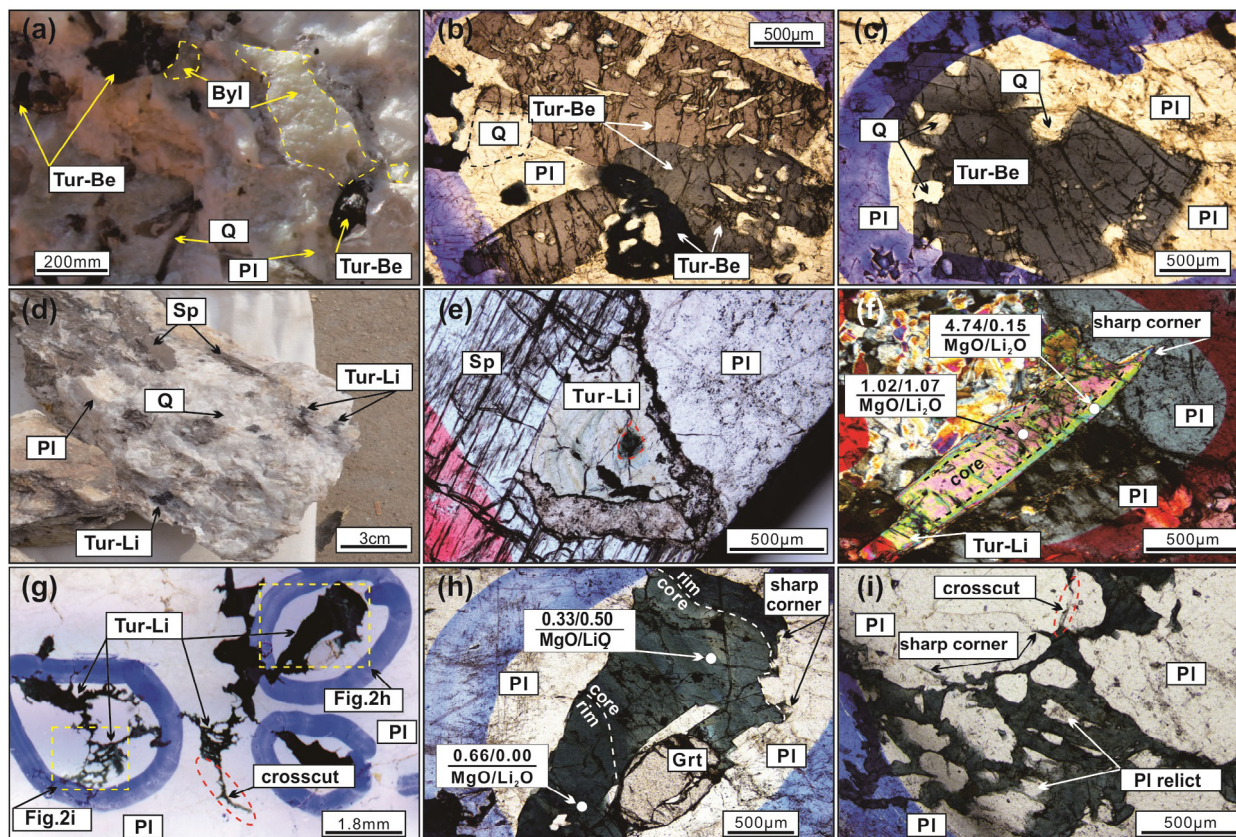
Fig. 2. Hand specimens and photomicrographs of Tur-Be and Tur-Li. **(a)** Hand specimen of beryl-bearing pegmatite. **(b, c)** Photomicrographs of Tur-Be crystals with homogenous optical color and containing abundant inclusions. **(d)** Hand specimen of spodumene-bearing pegmatite. **(e)** Photomicrograph of Tur-Li with irregular concentric optical zoning. **(f)** Photomicrograph of subhedral Tur-Li with irregular optical color zoning and sharp corner pointing toward plagioclase. **(g)** The photo of double polished thin section showing anhedral Tur-Li tourmalines with metasomatic texture. **(h)** Photomicrograph of subhedral Tur-Li crystal with irregular optical color zoning (blue in cores and dark-blue in rims). **(i)** Photomicrograph showing metasomatic textures between Tur-Li rim and plagioclase. The white circles in **(f)** and **(h)** are locations for EMPA analysis (circle size not in scale). The abundances of MgO (wt.%) and Li_2O (wt.%) are from the Supplementary Data Table S2. Q-quartz, Byl-beryl, Sp-spodumene, Pl-plagioclase, Grt-garnet, Tur-tourmaline.

thin section, the subhedral Tur-Li crystals show irregular concentric zoning (Fig. 2e, f) and the anhedral Tur-Li crystals display core-to-rim bluish color change (Fig. 2g–i). In both cases, the Tur-Li crystals do not contain mineral inclusions (Fig. 2e–i). The differences in color and texture between Tur-Be and Tur-Li indicate that they formed in different environments (Dutrow and Henry, 2011; van Hinsberg et al., 2011).

3.2. Analytical methods

In-situ analysis of Si, Ti, Al, Mn, Fe, Mg, Ca, Na, K, F and Cl contents for tourmaline was done at Wuhan SampleSolution Analytical Technology Co., ltd, using a JEOL JXA-8230 electron microprobe. A 15 kV accelerating voltage, a 20nA sample current and a 5 μm beam spot size was used for the analysis. Except for Ti, Mg and Mn (20 s and 10 s), peaks and backgrounds of the other elements were measured with 10 s and 5 s counting time, respectively. The analyses were corrected using the ZAF method with the following standards used: SiO_2 for Si, TiO_2 for Ti, $CaMnSi_2O_6$ for Ca, $NaAlSi_2O_6$ for Na, $(Mg, Fe)_2SiO_4$ for Mg, $Mg_3Al_2Si_3O_{12}$ for Al, $MnSiO_3$ for Mn, $(Mg, Fe)_2SiO_4$ for Fe, $KAlSi_3O_8$ for K, $Ca_5(PO_4)_3F$ for F and $Na_4BeAlSi_4O_{12}Cl$ for Cl. Based on the general formula of $XY_3Z_6[T_6O_{18}][BO_3]_3V_3W$ (Henry et al., 2011), the structural formula of the Tur-Be was calculated by normalizing to 15 cation atoms per formula unit (apfu) in the tetrahedral and octahedral sites ($T + Z + Y$). In addition, we calculated the structure formula of Tur-Li by assuming $^TSi = 6$ apfu, as documented in other Li-rich pegmatites worldwide (Jolliff et al., 1986).

Boron isotopic compositions of tourmalines were measured at the School of Earth and Space Sciences, Peking University, using a Nu Plasma II multiple coupled plasma-mass spectrometer (MC-ICP-MS) coupled with a Coherent Geolas HD 193 nm excimer laser ablation (LA) system. The spot size was set 60 μm. The laser fluence and repetition rates were 10 J/cm^2 and 5 Hz, respectively. The mass biases of the instrument and isotope fractionation were calibrated by the standard-sample-bracketing method using dravite as the external reference material and ^{29}Si measured from EMPA as the internal calibration. Schorl, elbaite and in-house reference material IMR RB1 were analyzed to assess the instrumental mass fractionation and measurement accuracy. The $\delta^{11}B$ values of schorl, elbaite and IMR RB1 in this study were −13.68‰ ± 0.32‰, −10.86‰ ± 0.44‰ and –13.92‰ ± 0.44‰ (2sd, $n = 8$), respectively, which agree with reported values within error (Xu et al., 2020). The above analyses of reference materials suggest negligible matrix effects. The final B-isotope analyses were reported relative to NIST SRM 951, and presented in a delta notation: $\delta^{11}B = [(^{11}B/^{10}B)_{sample}/(^{11}B/^{10}B)_{SRM951} − 1] \times 1000$.

4. Results

4.1. Mineral chemistry

A total of 74 EMPA analyses were done. The major element compositions of the Tur-Be and Tur-Li tourmalines are given in Supplementary Data Tables S1 and S2, respectively, and their average compositions are given in Table 2. The major element data

Table 2
Average compositions of tourmalines in the pegmatite veins from the CKBS deposit.

Element	Tur-Be core	Tur-Be rim	Tur-Li core	Tur-Li rim
SiO_2 (wt.%)	34.93	34.75	36.27	35.57
TiO_2	0.138	0.091	0.137	0.188
Al_2O_3	34.25	33.90	36.89	34.18
FeO	14.04	14.74	7.636	11.18
MnO	0.382	0.337	0.674	0.345
MgO	0.061	0.130	0.786	2.168
CaO	0.068	0.069	0.306	0.153
Na_2O	1.742	1.666	1.832	1.669
K_2O	0.039	0.036	0.023	0.034
Li_2O^*	0.018	0.006	0.706	0.065
F	0.251	0.143	0.416	0.060
Cl	0.002	0.003	0.004	0.007
$B_2O_3^*$	10.14	10.15	10.51	10.30
H_2O^*	3.380	3.432	3.427	3.524
Total	99.44	99.45	99.61	99.44
F = O	−0.106	−0.060	−0.175	−0.025
Cl = O	−0.001	−0.001	−0.001	−0.001
Total 2	99.34	99.38	99.44	99.41
Si (apfu)	5.984	5.952	6.000	6.000
Ti	0.018	0.012	0.017	0.024
Al	6.915	6.843	7.189	6.798
Fe	2.012	2.111	1.067	1.580
Mn	0.055	0.049	0.094	0.049
Mg	0.016	0.033	0.194	0.541
Mg/(Mg + Fe)	0.008	0.015	0.153	0.255
Ca	0.012	0.013	0.054	0.027
Na	0.579	0.553	0.586	0.546
K	0.008	0.008	0.005	0.007
Li	0.012	0.004	0.461	0.044
F	0.136	0.078	0.215	0.032
Cl	0.001	0.001	0.001	0.002
B	3.000	3.000	3.000	3.000
OH	3.863	3.921	3.784	3.966
O	27.00	27.00	27.00	27.00
T-site				
Si	5.984	5.952	6.000	6.000
Al	0.028	0.051	0.000	0.000
Z-site				
Al	6.000	6.000	6.000	6.000
Mg	0.000	0.000	0.000	0.000
Fe^{2+}	0.000	0.000	0.000	0.000
Y-site				
Al	0.887	0.792	1.189	0.798
Ti	0.018	0.012	0.017	0.024
Fe^{2+}	2.012	2.111	1.067	1.580
Mg	0.016	0.033	0.194	0.541
Mn	0.055	0.049	0.094	0.049
Li	0.012	0.004	0.461	0.044
X-site				
Ca	0.012	0.013	0.054	0.027
Na	0.579	0.553	0.586	0.546
Na/(Na + Ca)	0.979	0.978	0.920	0.953
K	0.008	0.008	0.005	0.007
X_{vac}	0.400	0.426	0.355	0.419
V + W-site				
F	0.136	0.078	0.215	0.032
OH	3.863	3.921	3.784	3.966
Cl	0.001	0.001	0.001	0.002

The values of H_2O^*, $B_2O_3^*$ and Li_2O^* were calculated according to the crystal structure of $XY_3Z_6T_6O_{18}(BO_3)_3V_3W$. More detailed calculations can be found in Supplementary Data Tables S1 and S2.

show that all the analyzed tourmalines belong to the alkali group (Fig. 3a). The Tur-Be tourmalines plot in the schorl field and display relatively homogeneous major element compositions from cores to rims, including lithium abundances (Fig. 3b, c; Table 2). The Tur-Be tourmalines have high Na/(Na + Ca) ratios (0.963–0.998), high Al contents on the *Y* site (0.661–0.995 apfu), and low Mg/(Fe + Mg) ratios (0.005–0.025), which are similar to the major element compositions of magmatic tourmalines in granite-pegmatite systems (e.g., London and Manning, 1995; Zhao et al., 2019; Cheng et al.,

2021). In contrast to Tur-Be, the cores and rims of Tur-Li tourmalines show obvious chemical differences without continuous evolution tendencies (Fig. 3b, c). The abundances of lithium in the Tur-Li tourmalines decrease from cores to rims (Fig. 2f, h and 3b; Table 2). Meanwhile, the cores of Tur-Li are consistent with tourmalines in Li-rich granitoids, pegmatites and aplites on the Al-Fe-Mg ternary, whereas Tur-Be and the rims of Tur-Li plot mainly in the Li-poor region (Fig. 3c). Furthermore, the rims of Tur-Li show higher average Fe, Mg, Na/(Na + Ca), Mg/(Mg + Fe), $X_{vacancy}$, and lower average Li and Al abundances than the cores (Table 2).

4.2. Boron isotope composition

A total of 16 spots were analyzed for boron isotope compositions of the tourmalines. The analytical spots are at or spatially close to those spots analyzed for major element. The B isotope data are given in Table 3. The $\delta^{11}B$ values of all the tourmaline crystals vary from −13.33‰ to −12.27‰ with standard error of ± 0.04‰ to ± 0.08‰ (Table 3), which is similar to those of S-type granite worldwide (−11‰ ± 4‰, Trumbull and Slack, 2018). The $\delta^{11}B$ values of Tur-Be range from −13.33‰ to −12.36‰ (average = −12.85‰). The $\delta^{11}B$ values in the rims of Tur-Be are lower than that of corresponding cores by 0.09‰ to 0.94‰ (Table 3). Tur-Li shows a slightly higher average $\delta^{11}B$ value (−12.47‰) than Tur-Be (−12.85‰). In striking contrast to Tur-Be, the $\delta^{11}B$ values of Tur-Li tend to show a core-to-rim increase. The difference of $\delta^{11}B$ value between the cores and rims of Tur-Li is up to 0.41‰ (Fig. 5a, b), which far exceeds the analysis error (Table 3).

5. Discussion

5.1. Origin of tourmalines

The subhedral to euhedral Tur-Be crystals are texturally isolated and dispersed in the beryl-bearing pegmatite (Fig. 2a). There is no textural evidence for their replacement of pre-existing phases or being metasomatized by exotic fluids. In contrast, the Tur-Be crystals coexist with rock-forming mineral grains of quartz and plagioclase with sharp and planar contacts (Fig. 2a−c), suggesting that they formed during the crystallization of the rock-forming minerals. Hence, these tourmalines most likely formed as the result of *syn*-magmatic crystallization from a boron-rich melt, i.e., a magmatic origin. The Tur-Be tourmalines are morphologically similar to tourmalines in leucogranite (Zhou et al., 2019; Cheng et al., 2021), which were suggested to have a *syn*-magmatic origin. The *syn*-magmatic origin of Tur-Be is further supported by high Na/(Na + Ca) ratios (0.963–0.998) and ^YAl contents (0.661–0.995 apfu), and low Mg/(Fe + Mg) ratios (0.005–0.025) (Supplementary Data Table S1), which are considered to be geochemical characteristics of *syn*-magmatic tourmalines (e.g., London and Manning, 1995; da Costa et al., 2014; Zhao et al., 2019; Cheng et al., 2021; Guo et al., 2022). In conclusion, both texture and major element compositions indicate that the Tur-Be tourmalines directly crystallized from a B-rich melt.

The Tur-Li tourmalines in the spodumene-bearing pegmatites are mainly anhedral with some being subhedral. Different from Tur-Be, the subhedral Tur-Li crystals commonly show irregular/annular zoning (Fig. 2e, f) whereas the anhedral Tur-Li grains generally display blurred irregular patchy zoning (core-to-rim bluish color change, Fig. 2g−i). In both cases, the cores of the Tur-Li tourmalines have higher Li_2O and lower MgO abundances than the corresponding rims (Fig. 2f, h). The compositional and optical contrasts indicate that the cores and rims of the Tur-Li tourmalines formed under different environments (Dutrow and Henry, 2011; van Hinsberg et al., 2011). Plagioclase is obviously a liquidus phase
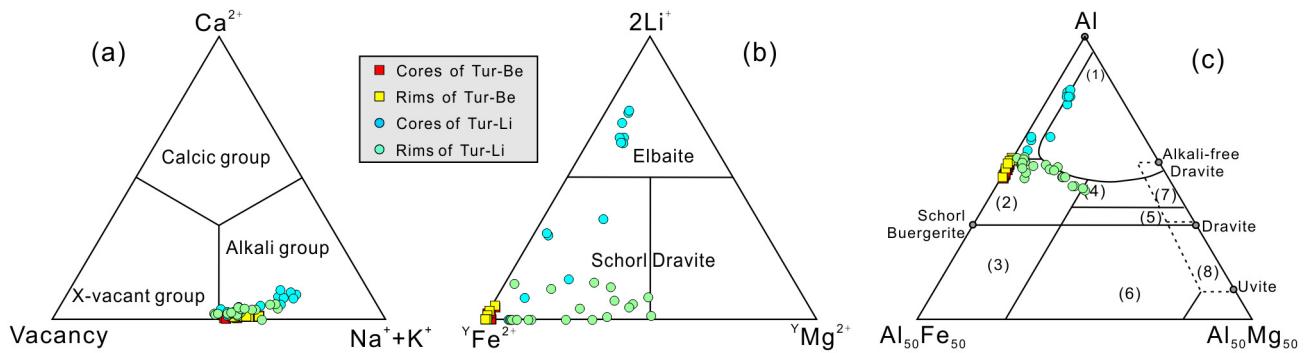
Fig. 3. Overview of tourmaline compositions in the pegmatite veins from the CKBS Li-Be deposit. **(a)** Tourmaline classification in terms of X-site occupancy (Hawthorne and Henry, 1999). **(b)** Tourmaline classification using Y-site occupancy to distinguish the alkali type tourmalines (Hawthorne and Henry, 1999). **(c)** Tourmaline classification of Al-Fe-Mg compositions (Henry and Guidotti, 1985), where the labeled fields are: (1) Li-rich granitoids, pegmatites, and aplites; (2) Li-poor granitoids, pegmatites, and aplites; (3) Fe^{3+}-rich quartz-tourmaline rocks (altered granitoids); (4) metapelites and metapsammites with Al-saturating phase; (5) metapelites and metapsammites lacking Al-saturating phase; (6) Fe^{3+}-rich quartz-tourmaline rocks, calcsilicate rocks, and metapelites; (7) low-Ca metaultramafic rocks and Cr-V-rich metasediments and (8) metacarbonates and meta- pyroxenites.
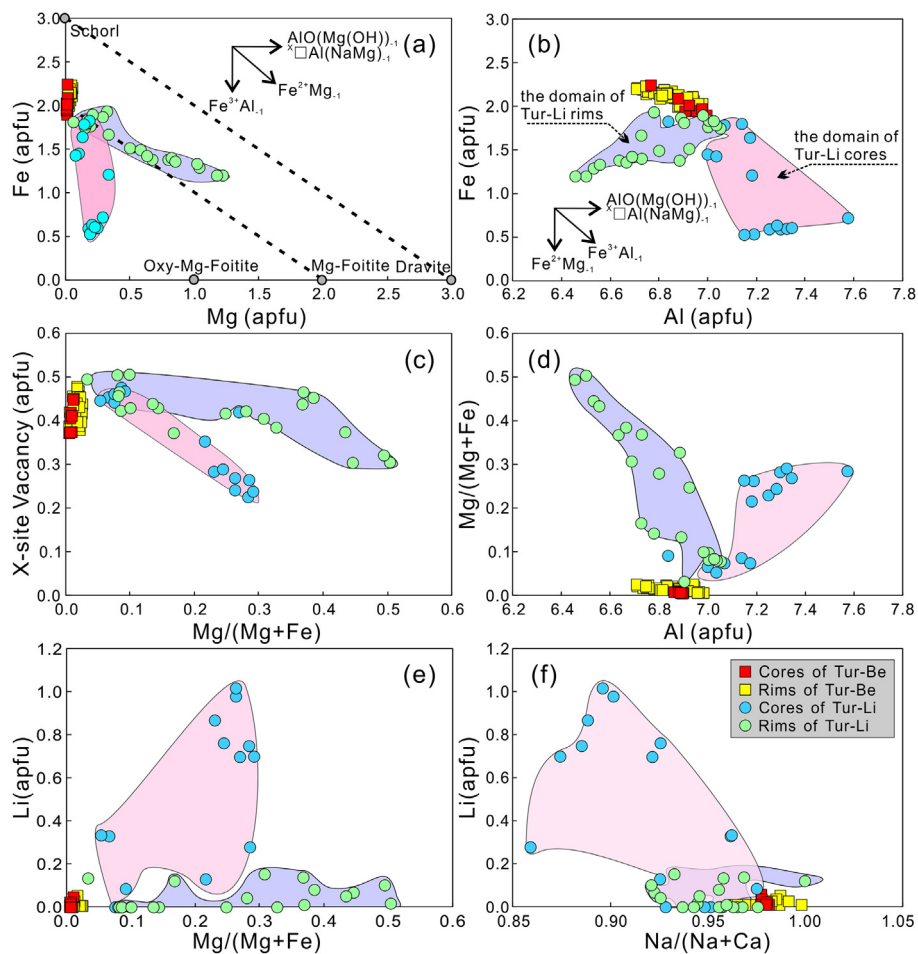

Fig. 4. Chemical compositions of tourmalines in the pegmatite veins from the CKBS deposit expressed in terms of (a) Mg (apfu) vs Fe (apfu), (b) Al (apfu) vs Fe (apfu), (c) Mg/(Mg + Fe) vs X-site vacancy (apfu), (d) Al (apfu) vs Mg/(Mg + Fe), (e) Mg/(Mg + Fe) vs Li (apfu) and (f) Na/(Ca + Na) vs Li (apfu). Data are given in Supplementary Data Tables S1 and S2. The arrows in the (a and b) depict the substitution trend of major element compositions (Qiu et al., 2021), wherein the black rectangle represents the vacancy on X-site. The areas with baby blue and baby pink in the (a–f) represent the domains of the cores and rims of Tur-Li, respectively.

crystallized from pegmatite-forming melts (London, 2018). Thus, the phenomena of crosscut plagioclase along with microcracks with sharp corners pointing toward plagioclase and containing plagioclase relics (Fig. 2f–i) indicate that the rims of Tur-Li crystals have a hydrothermal origin, which is generally considered to be correlated with the exsolution, separation and entrapment of an immiscible aqueous Na-Fe-B-rich fluid (Pichavant, 1981; Zhou et al., 2019). The exsolved liquid is saturated in tourmaline when it acquires Al cation from the existing feldspars (Fig. 2f–i, e.g., Trumbull et al., 2008; Drivenes et al., 2015; Zhou et al., 2019;

Table 3
The Boron isotope analyses results of tourmalines.

Analysis No.	Sample No.	Type	Domain No.	$\delta^{11}B$ (‰)	SE
1	CK2008-4	Tur-Be	1Core	−13.06	0.04
2	CK2008-4	Tur-Be	1Rim	−13.20	0.04
3	CK2008-4	Tur-Be	1Rim	−13.15	0.04
4	CK2008-6	Tur-Be	1Rim	−12.98	0.05
5	CK2008-6	Tur-Be	1Core	−12.39	0.05
6	CK2008-6	Tur-Be	1Rim	−13.33	0.08
7	CK2008-6	Tur-Be	2Core	−12.36	0.06
8	CK2008-6	Tur-Be	2Core	−12.37	0.05
9	CK2008-6	Tur-Be	2Rim	−12.80	0.06
10	CK2003-4	Tur-Li	1Core	−12.65	0.05
11	CK2003-4	Tur-Li	1Rim	−12.40	0.04
12	CK2003-4	Tur-Li	1Rim	−12.33	0.04
13	CK2007-2	Tur-Li	1Core	−12.68	0.04
14	CK2007-2	Tur-Li	1Rim	−12.64	0.04
15	CK2007-2	Tur-Li	1Rim	−12.30	0.04
16	CK2007-2	Tur-Li	1Rim	−12.27	0.04

Zhao et al., 2021). Considering the difference in optical colors (Fig. 2e−i) and the discontinuous evolution tendency in major element compositions (Fig. 4) and the fact of cores forming earlier than the corresponding rims, we suggest that the cores of Tur-Li most likely formed as the result of magmatic crystallization, i.e., hydrothermal rims overgrow on magmatic cores. The fact that the rims of Tur-Li with large chemical variation developed around relatively homogeneous cores (Figs. 3, 4) is similar to the observation of hydrothermal tourmalines overgrowths on magmatic tourmalines in the Cornubian granite (London and Manning, 1995). The two-stage origin model for Tur-Li is further supported by the observation that the average abundance of FeO (7.636 wt.%) in the cores of Tur-Li is an order of magnitude lower than that in the rims of Tur-Li (11.18 wt.%, Table 2). Iron element (Fe) is a fluid-mobile element (McNeil et al., 2020). Thus, the hydrothermal rims of Tur-Li resulting from exsolved fluids show higher FeO than the corresponding cores crystallized directly from melts. The B-isotopic compositions in the cores and rims of the Tur-Li crystals also support the two-stage origin model (see below).

5.2. Boron isotope fractionation and pegmatite evolution

Boron has two isotopes with ^{11}B preferring trigonal coordination and ^{10}B favoring tetrahedral coordination (e.g., Ribacki et al., 2022; Smith and Yardley, 1996; Trumbull et al., 2013). Several studies of B isotopes on tourmalines in granites and pegmatites have been reported (e.g., Drivenes et al., 2015; Trumbull and Slack, 2018; Zhou et al., 2019; Cheng et al., 2021), but B isotopes in tourmalines from Be-rich and Li-rich pegmatite veins in one pegmatite field need studying and understanding. In the CKBS deposit, we found opposite core-to-rim B isotope variation trends between Tur-Be and Tur-Li, where $\delta^{11}B$ decreases from core to rim in Tur-Be, but increases from core to rim in Tur-Li (Table 3; Fig. 5a−d).

Before attempting to interpret the cause of the observed boron isotope fractionation in Tur-Be and Tur-Li, it is necessary to review the factors that may affect B-isotope fractionation in a pegmatite context. In principle, the B isotope fractionation in a hydrous granitic melt is dependent mainly on temperature and boron coordination environment (Hervig et al., 2002; Wunder et al., 2005; Meyer et al., 2008; Trumbull and Slack, 2018; Cheng et al., 2022). Since pegmatite has an isothermal crystallization history revealed by the feldspar thermometer (London, 2018; London et al., 2020), the fractionation of ^{11}B and ^{10}B in the pegmatite-system is controlled mainly by the proportion of B^{III}/B^{IV} in the melt, fluid and mineral phases (e.g., Siegel et al., 2016; Cheng et al., 2021). Tourmaline and muscovite are two major B-bearing minerals in peg-

matite. Boron coordination is trigonal in tourmaline whereas tetrahedral in muscovite. Therefore, there is no doubt that a large B isotope fractionation exists when the two minerals coexist (e.g., Wunder et al., 2005; Meyer et al., 2008; van Hinsberg et al., 2011; Trumbull et al., 2013). However, the B isotope fractionation between B-bearing minerals (tourmaline, muscovite) and magma is highly uncertain because boron in the silicate magma occupies both trigonally and tetrahedrally coordinated sites and the relative proportions of which depend on several factors including water content, aluminum to alkali ratio, pressure and the concentration of boron (Tonarini et al., 2003; Cheng et al., 2021; Zhao et al., 2021 and references therein). Recently, experimental and case studies have testified that the fractionation factors both for melt-tourmaline and melt-muscovite in a pegmatite context are positive (e.g., Siegel et al., 2016; Cheng et al., 2022), and the former can be quantitatively expressed as $\Delta^{11}B_{melt-tourmaline} = 4.51 \times (1000/T [K]) - 3.94$ (Cheng et al., 2022). In contrast to silicate melt, it is well established that trigonal $B(OH)_3$ complex is the predominant boron species in fluids at crustal level magmatic temperature conditions regardless of their pH (e.g., Cheng et al., 2021; Schmidt et al., 2005), and the fluids are always more enriched in ^{11}B relative to the hydrous granitic melts and B-bearing minerals (e.g., Palmer et al., 1992; Hervig et al., 2002; Wunder et al., 2005; Meyer et al., 2008; Maner and London, 2018; Chakraborty, 2021). Furthermore, experimental studies have proposed that the fractionation factors of tourmaline-fluid and mica/melt-fluid could be expressed as $\Delta^{11}B_{tourmaline-fluid} = -4.20 \times [1000/T (K)] + 3.52$ (Meyer et al., 2008) and $\Delta^{11}B_{muscovite/melt-fluid} = -10.69 \times [1000/T (K)] + 3.88$ (Wunder et al., 2005), respectively.

Based on the above considerations, two possible models could account for the decreased core-to-rim $\delta^{11}B$ values of Tur-Be in this study: a phase removing ^{11}B from the pegmatite-forming melt or a new melt phase inputting ^{10}B into the pegmatite-forming melt. If the latter is the case, the major element composition of the tourmalines should display chemical zoning, which is contrary to the observation of Tur-Be (Figs. 3, 4). Due to the absence of experimental determination, previous studies suggest that tourmalines could effectively remove ^{11}B from hydrous granitic melts, resulting in heavy B isotope decrease in the residual melts along with gradual crystallization fractionation (e.g., Trumbull et al., 2013; Drivenes et al., 2015; Zhao et al., 2019). However, a recent experimental study has proved that the B fractionation factor between hydrous granitic melt and tourmaline is positive as discussed above (Cheng et al., 2022), i.e., the $\delta^{11}B$ value in the residual granitic melt gradually increases with continued tourmaline crystallization as shown by the short red dotted line in Fig. 6. Therefore, the most realistic mechanism responsible for producing the observed boron
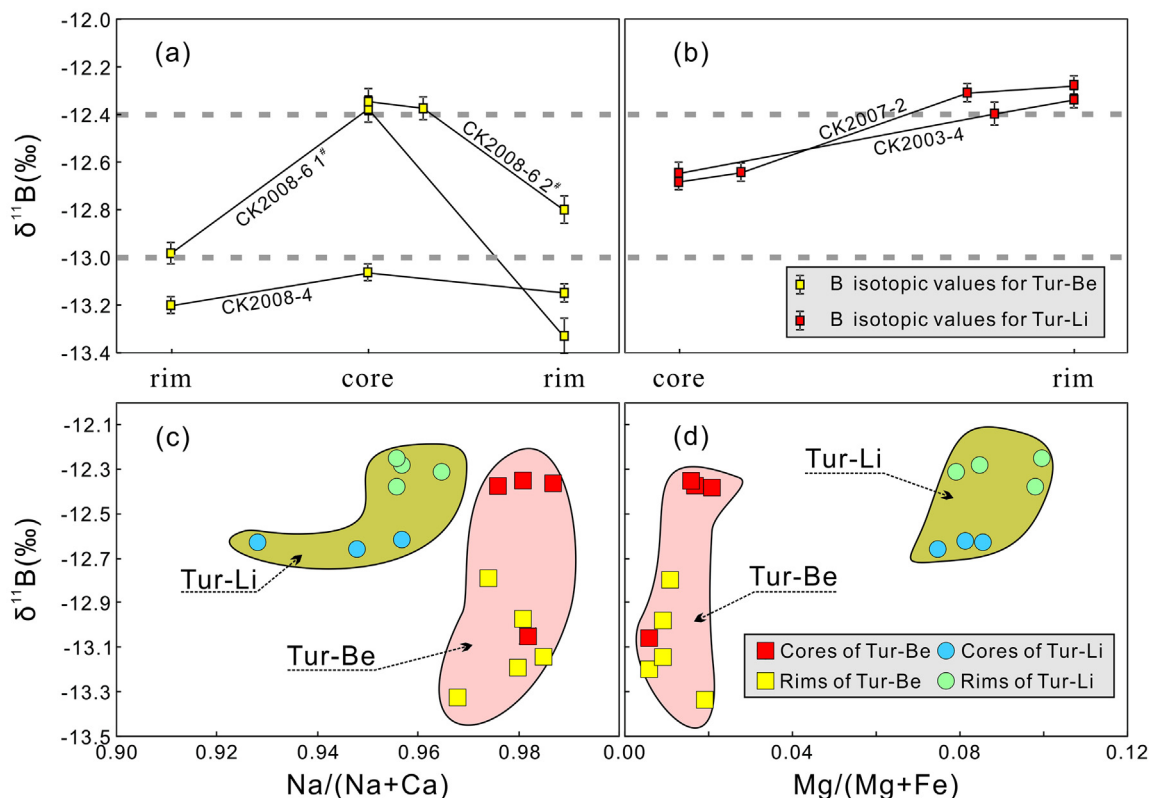
Fig. 5. **(a)** The B-isotope variations of the Tur-Be tourmalines from cores to rims; **(b)** B-isotope variations of the Tur-Li tourmalines from cores to rims; **(c)** plot diagram of δ^{11}B vs. Na/(Na + Ca); **(d)** plot diagram of δ^{11}B vs. Mg/(Mg + Fe). The B-isotope data are given in Table 3. The Na/(Na + Ca) and Mg/(Mg + Fe) ratios are given in Supplementary Data Tables S1 and S2.

isotopic fractionation trend in Tur-Be is that an escaped aqueous vapor/fluid phase took ^{11}B away from the residual melt, as documented in the Sinceni pegmatite (Trumbull and Chaussidon, 1999), Varutrask pegmatite (Siegel et al., 2016), Conadong leucogranite (Cheng et al., 2021), Erongo granite (Trumbull et al., 2008), Penamacor-Monsanto granite (da Costa et al., 2014) and Cligga Head granite (Smith and Yardley, 1996). The event of aqueous vapor/fluid phase escape is further supported by the following two reasons. First, the B abundances of beryl-bearing pegmatite veins in the CKBS deposit are 24–100 ppm (Wang et al., 2020a), which is lower than that required for tourmaline crystallization in hydrous pegmatitic melts (*ca.* 311 ppm at 500 °C, London 2011), indicating B transfer into the exsolved fluid/vapor phase (da Costa et al., 2014). Second, we calculated the theoretical amount of H_2O in the beryl-bearing pegmatite based on the relationship between ASI and H_2O in a granitic melt in equilibrium with tourmalines (ASI = 1.104 + 0.049×H_2O, Acosta-Vigil et al., 2003), indicating 12–87 wt.% H_2O loss by comparing these values with the actual H_2O content in the sampled beryl-bearing pegmatite (H_2O = 0.59–0.78 wt.%, ASI = 1.15–1.32, Wang et al., 2020a). Furthermore, considering the homogeneous major element compositions (Figs. 3, 4) and the lack of clear correlation between B isotope and major elements in Tur-Be (Fig. 5c, d), it can be reasonably deduced that the escaped ^{11}B-rich phase is dominated by volatile (e.g., H_2O, $B(OH)_3$, F) with other components being negligible, i.e., loss of ^{11}B by degassing (Jiang and Palmer, 1998; Beurlen et al., 2011). To quantitatively evaluate the effect of degassing on the B isotope change of Tur-Be, we have done simple calculations (Fig. 6), which illustrates that removal of ∼ 28% B by degassing can explain the core-to-rim B isotope drop of Tur-Be.

The markedly different core-to-rim boron isotope fractionation trends of Tur-Be and Tur-Li (Fig. 5a, b) suggest that the boron iso-

tope fractionation in the latter cannot be explained by magma degassing. Crystallization of muscovite and/or early tourmaline is a potential mechanism explaining the increased δ^{11}B value from core to rim in Tur-Li (Trumbull et al., 2013; Siegel et al., 2016; Cheng et al., 2022). However, muscovite/early-tourmaline crystallization cannot explain the discontinuity of major element between the cores and rims of Tur-Li (Figs. 3, 4). Hydrothermal tourmaline overgrowth on magmatic tourmaline is another potential mechanism for producing increased core-to-rim δ^{11}B values, since the exsolved fluid and any hydrothermal tourmaline formed from it will be isotopically heavier than the starting magma due to different boron coordination between fluids (B^{III}) and melts (B^{IV}) (Trumbull and Slack, 2018; Zhao et al., 2021). Together with the major element and textural characteristics of Tur-Li as discussed above, we suggest that the boron isotopic variation of Tur-Li is a passive record of crystallization environment changes, i.e., B-isotope compositions of the cores derived from the parental hydrous silicate melt whereas that of the rims inherited from the fluid exsolved from the residual hydrous silicate melt after the magmatic core crystallization. Similar observations and conclusions have been made for tourmalines in hydrous granitic melts elsewhere (e.g., Trumbull et al., 2013; Drivenes et al., 2015).

5.3. Implications for pegmatite origin

5.3.1. Fractional crystallization vs partial melting

Several studies have shown that boron isotope compositions of early crystallized magmatic tourmalines can be used to estimate the δ^{11}B value of melts parental to magmatic rock (e.g., Zhao et al., 2019; Cheng et al., 2021). According to the experimental studies on boron isotope fractionation between hydrous granitic melt and tourmaline (Cheng et al., 2022) and case studies of the

feldspar thermometer in pegmatite (London, 2018), we assume that the tourmalines in the CKBS pegmatite veins crystallized at 500 °C with $\Delta^{11}B_{melt-tourmaline}$ value = +1.9. Combined with the extreme $\delta^{11}B$ value of the magmatic cores of Tur-Be (−12.36‰) and Tur-Li (−12.68‰), it is estimated that the $\delta^{11}B$ values of initial melts of the beryl-bearing and spodumene-bearing pegmatite to be ∼ −10.46‰ and ∼ −10.78‰, respectively. These boron isotopic compositions are informative on the origin of the beryl-bearing and spodumene-bearing pegmatite veins (e.g., Trumbull and Slack, 2018; Zhou et al., 2019).

Previous studies have interpreted pegmatite veins with regional zonation as resulting from protracted differentiation of granitic magmas (e.g., Černý, 1991; Hulsbosch et al., 2014; London, 2018; Yan et al., 2020; Raschke et al., 2021; Siani et al., 2021; Sun et al., 2021; Troch et al., 2022) or from low degree melting of meta-pelite (e.g., Müller et al., 2015; Chen et al., 2020; Chukwu and Obiora, 2021). The latter interpretation infers that the residual phases in the source region of Li-poor pegmatite are characterized by more biotite than muscovite whereas those of Li-rich pegmatite are dominated by muscovite over biotite (Chen et al., 2020). Muscovite, as a major B-bearing mineral in metapelite, favors ^{10}B over ^{11}B (Wunder et al., 2005; Trumbull and Slack, 2018). As a result, the initial melt of the Li-rich pegmatite would have a higher $^{11}B/^{10}B$ than that of the Li-poor pegmatite because more ^{10}B is retained by muscovite in the source region. Accordingly, if the CKBS rare metal pegmatite veins were derived from partial melting of metapelite, the $\delta^{11}B$ value of initial melts of the spodumene-bearing pegmatite veins (Li-rich, Li = 9105–12,354 ppm, Wang et al., 2020a) would be higher than that of the beryl-bearing pegmatite veins (Li-poor, Li = 38–46 ppm, Wang et al., 2020a). However, quantitative calculations suggest that the initial melts of the beryl-bearing pegmatites have heavier B (i.e., higher $\delta^{11}B$ values of ∼ − 10.46 ‰) than that of the spodumene-bearing pegmatite (∼−10.78‰). Thus, the CKBS rare metal pegmatite veins most likely result from protracted fractional crystallization/differentiation of granitic intrusions rather than partial melting of meta-

pelite. This is further supported by boron isotope compositions of the tourmalines from the CKBS deposit that agree well with those in other granite-related pegmatites (Fig. 7), such as tourmalines in the Sanfeng granite-pegmatite (Zhao et al., 2019), Sinceni granite-pegmatite (Trumbull and Chaussidon, 1999), Nattaung granite-pegmatite (Li et al., 2020) and Varutrask pegmatite (Siegel et al., 2016). Except for B isotope compositions in the tourmalines, the increasing Li-Be contents of bulk-rock from barren through beryl-bearing to spodumene-rich pegmatites, and the decreasing K/Rb ratios coupling with increasing Cs contents in the K-feldspar and muscovite, also support the conclusion that the rare metal pegmatites in the CKBS deposit are derived from fractional crystallization of granitic magmas (Liu et al., 2023). Numerous 250–235 Ma granitoids exposed around the CKBS deposit (Huang et al., 2014; Shao et al., 2017; Pan et al., 2021) indicate that there existed extensive granitic magmatism in the region during the Early-Middle Triassic, which was very favorable for the formation of the coeval pegmatites (∼240 Ma, Pan et al., 2021) in the CKBS deposit.

5.3.2. Degree of pegmatite-forming melt differentiation

The major element compositions in the cores of the two-type tourmalines are different (Figs. 3, 4), indicating that the melts parental to the two pegmatites are different or the initial melts from which the two types of tourmalines crystallized are different. The latter scenario may be more likely and represent melts of different
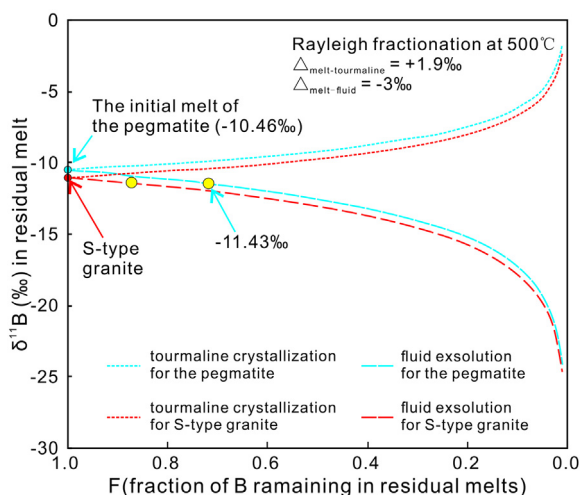
Fig. 6. Modeled curves illustrating the change of $\delta^{11}B$ values for residual melt of the beryl-bearing pegmatite and S-type granite as the result of tourmaline crystallization and a fluid phase exsolution, assuming Rayleigh fractionation. Calculations are conducted for 500 °C, which is the expected highest solidus temperature of pegmatite (London, 2018). The $\delta^{11}B$ value at F = 1.0 for the initial melt of the beryl-bearing pegmatite is −10.46‰ (see text for details) and for S-type granite is −11‰ (Trumbull and Slack, 2018), respectively. The fractionation factors of melt-tourmaline is calculated using $\Delta^{11}B_{melt-tourmaline}$ = 4.51 × [1000/T(K)] − 3.94 (Cheng et al., 2022). The $\Delta^{11}B_{melt-vapor/fluid}$ value shown is estimated at −3‰ at 500 °C following Trumbull et al. (2013). The yellow circles represent $\delta^{11}B$ values of residual melts at the end of Tur-Be crystallization, calculated from the $\delta^{11}B$ values determined at the rim of the Tur-Be tourmalines.
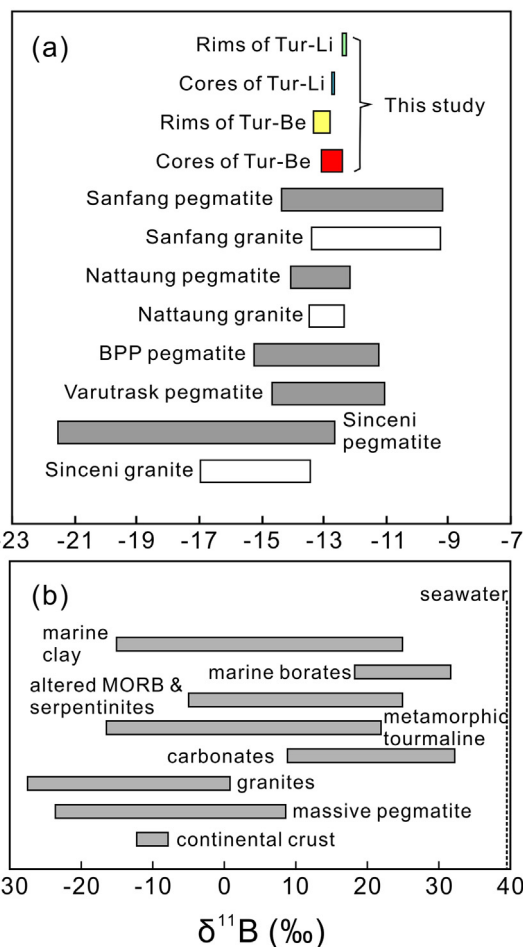
Fig. 7. Summary of B isotope compositions for tourmalines in the pegmatite veins from the CKBS Li-Be deposit and from other granite-related pegmatites (a), and for global boron reservoirs (b). Data sources in (a): Table 3, Trumbull and Chaussidon (1999), Beurlen et al. (2011), Siegel et al. (2016), Zhao et al. (2019) and Li et al. (2020). Data sources in (b): Palmer and Swihart (1996), Xiao et al. (2013).
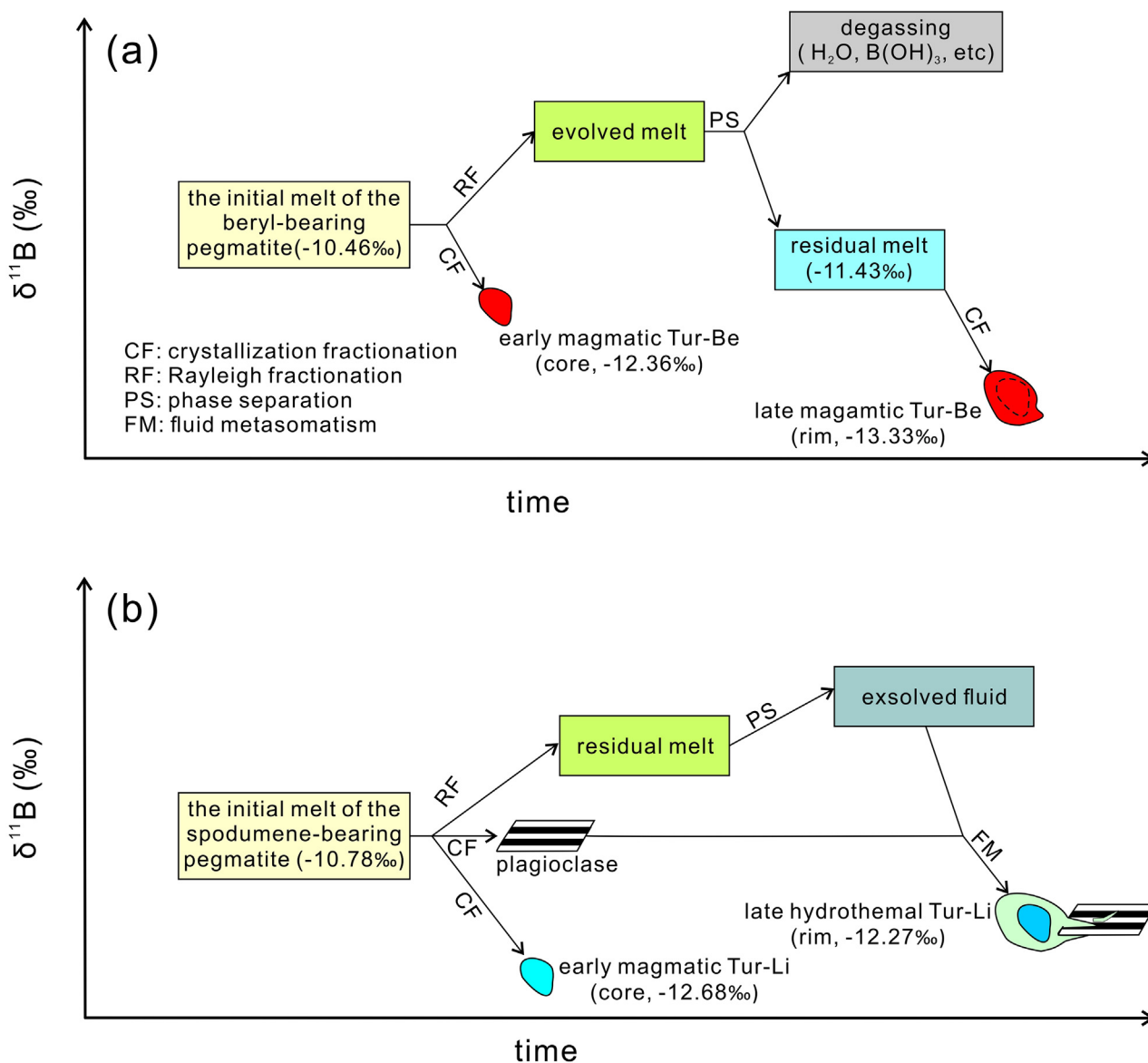
Fig. 8. A graphic summary for the formation of tourmaline, pegmatite and boron isotope fractionation. (**a**) For Tur-Be and the beryl-bearing pegmatite; (**b**) for Tur-Li and the spodumene-bearing pegmatite. See text for details.

evolution histories/stages, as described in the regionally zoned pegmatite veins elsewhere in the world (e.g., Černý, 1991; Hulsbosch et al., 2014; Zhou et al., 2022). The following two observations from the CKBS deposit further confirm that the degree of pegmatite-forming melt differentiation progressively increases from the beryl-bearing pegmatite to the spodumene-bearing pegmatite. First, there is no statistically significant correlation between Li and Mg/(Mg + Fe) or Na/(Ca + Na) ratios (Fig. 4e, f), implying that Li is predominantly controlled by melt/fluid compositions rather than crystallographic structure, i.e., Li in the two-type tourmalines can be used to trace the changes in the composition of the melt/fluid from which the tourmaline crystallized (Zhao et al., 2019; Zhao et al., 2021; Guo et al., 2022). The average Li_2O concentration of the Tur-Li cores (0.706 wt.%, Table 2) is higher than that of the Tur-Be cores (0.018 wt.%), suggesting that the lithium content in the initial melt of the spodumene-bearing pegmatite is higher than that of the beryl-bearing pegmatite, which is suggestive of increasing chemical fractionation because Li becomes increasingly enriched in the residual melt along with granitic mag-

mas undergoing cooling and crystallization (Sun et al., 2022; Troch et al., 2022). Second, the NaCl content in hydrous melts/fluids is expected to exert a strong control on the composition of tourmaline, in addition to the bulk composition, *P-T* conditions and crystallization sequence among others (Chakraborty, 2021). Experimental studies have testified that Fe can readily form bonds with chlorine to form complexes in highly saline fluids (e.g., Ding and Seyfried, 1992; Orlando et al., 2017), resulting in the crystallization of Mg-rich tourmalines in the hydrous granitic melt (Chakraborty, 2021). The average Mg/(Mg + Fe) ratio of magmatic Tur-Be cores (0.008) is approximately two order of magnitude lower than that of the Tur-Li cores (0.153, Table 2), indicating that the hydrous granitic melt from which the Tur-Be cores crystallized has lower salinity than the melt in which the Tur-Li tourmaline cores formed. This supports the idea that the initial melt of the spodumene-bearing pegmatite is chemically more evolved than that of the beryl-bearing pegmatite because the salinity of the residual hydrous melts increases with progressive cooling and crystallization of granitic magma systems.

According to the above discussion, a genetic model of tourmaline formation, pegmatite evolution and associated boron isotopic fractionation is illustrated in Fig. 8. In brief, the origin of the regionally zoned pegmatite veins in the CKBS deposit is best understood as resulting from crystallization/differentiation of granitic magmas. After the pegmatite-forming melts emplaced into shallow crust, they experience different evolution histories. The key steps are as follows:

(1) The $\delta^{11}B$ value in the initial melt of the beryl-bearing pegmatite is $\sim -10.46‰$. Tur-Be crystallizes directly from the silicate melt. During Tur-Be crystallizes, an aqueous vapor phase is lost resulting in the $\delta^{11}B$ value of Tur-Be changing from $-12.36‰$ in core to $-13.33‰$ in rim (Fig. 8a).

(2) The $\delta^{11}B$ value in the initial melt of the spodumene-bearing pegmatite is $\sim -10.78‰$. The melt experiences a complex evolution history from magmatic stage to hydrothermal stage. The cores of Tur-Li with $\delta^{11}B$ of $-12.68‰$ crystallize at magmatic stage. Along with the crystallization of magmatic cores of Tur-Li, a fluid phase is exsolved from the residual melt because the crystallization of the magmatic Tur-Li cores consumes a large amount of B_2O_3 and sharply lowers the solubility of water in the residual melt (Pichavant, 1981; Holtz et al., 1993). The exsolved fluid metasomatizes plagioclase and results in overgrowth of Tur-Li rims with heavier B-isotope ($-12.27‰$) on the cores with lighter B-isotope (Fig. 8b).

6. Conclusions

The Tur-Be and Tur-Li tourmalines show clear differences in texture, and major element and B-isotopic compositions. The Tur-Be tourmalines are homogeneous schorls as *syn*-magmatic crystallization products. An aqueous vapor phase is lost during the evolution of the melt parental to the beryl-bearing pegmatite, resulting in Tur-Be core-to-rim $\delta^{11}B$ drop, which is further supported by the quantitative calculations of bulk-rock H_2O and B abundances. The Tur-Li tourmalines are formed via two stages: the crystal cores (mostly elbaite and Li-rich schorl with subordinate schorl) are of magmatic origin and the crystal rims (schorl) are of hydrothermal origin. The discontinuous core-to-rim change of major element compositions and the core-to-rim $\delta^{11}B$ value increases in the Tur-Li crystals result from fluid exsolution. According to B isotope compositions in the cores of Tur-Be and Tur-Li crystals, we calculate the B isotope compositions in the initial melts of beryl-bearing and spodumene-bearing pegmatites and suggest that the pegmatite veins in the CKBS deposit are products of extreme differentiation of granitic magmas rather than partial melting of metapelite. The Mg/(Mg + Fe) ratios and Li abundances in the cores of the Tur-Li tourmalines are higher than those of the Tur-Be tourmalines, revealing that the degree of pegmatite-forming melt fractionation increases from the beryl-bearing pegmatite to the spodumene-bearing pegmatite.

CRediT authorship contribution statement

Wenli Sun: Conceptualization, Data curation, Investigation, Writing – original draft. **Zhidan Zhao:** Conceptualization, Investigation, Project administration, Funding acquisition, Writing - review & editing. **Yaoling Niu:** Conceptualization, Writing - review & editing. **Chunjing Wei:** Supervision. **Guochen Dong:** Investigation, Project administration. **Xiaowei Li:** Project administration. **Wanming Yuan:** Investigation, Project administration. **Tao Wang:** Investigation, Project administration. **Bingzhang Wang:** Investigation, Supervision. **Tong Pan:** Supervision. **Jie Han:** Investigation. **Hongliang Cao:** Investigation. **Yan Tang:** Investigation. **Dicheng Zhu:** Supervision.

Declaration of Competing Interest

The authors declare that they have no known competing financial interests or personal relationships that could have appeared to influence the work reported in this paper.

Appendix A. Supplementary data

Supplementary data to this article can be found online at https://doi.org/10.1016/j.gsf.2023.101611.

References

Acosta-Vigil, A., London, D., Morgan, G.B., Dewers, T.A., 2003. Solubility of excess alumina in hydrous granitic melts in equilibrium with peraluminous minerals at 700–800 °C and 200 MPa, and applications of the aluminum saturation index. Contrib. Mineral. Petr. 146, 100–119.

Baker, D.R., 1998. The escape of pegmatite dikes from granitic plutons: constraints from new models of viscosity and dike propagation. Can. Mineral. 36, 255–263.

Beurlen, H., Trumbull, R.B., Wiedenbeck, M., Soares, D.R., 2011. Boron-isotope variations in tourmaline from granitic pegmatites of the Borborema Pegmatite Province, NE-Brazil. Asociación Geológica Argentina, Serie D, Publicación Especial 14, 37–39.

Bosi, F., 2018. Tourmaline crystal chemistry. Am. Mineral. 103, 298–306.

Černý, P., 1991. Rare-element granitic pegmatites. Part II: Regional to global environments and petrogenesis. Geosci. Can. 18, 68–81.

Chakraborty, T., 2021. Tourmaline growth and evolution in S-type granites and pegmatites: constraints from textural, chemical and B-isotopic study from the Gangpur Schist Belt granitoids, eastern India. Geol. Mag. 158, 1657–1670.

Chen, J., Han, J., Yu, F.C., Wang, B.Z., Li, W.F., 2022. ^{40}Ar-^{39}Ar dating of muscovite in Chaka Beishan Li-polymetallic deposit in Qinghai Province and the geological significance. Contrib. Geol. Mineral. Resour. Res. 37(2), 142-147 (in Chinese with English abstract).

Chen, B., Huang, C., Zhao, H., 2020. Lithium and nd isotopic constraints on the origin of li-poor pegmatite with implications for li mineralization. Chem. Geol. 551, 119769.

Chen, N.S., Lu, Z., Min, S., Wang, Q.Y., Kusky, T.M., 2012. U-Pb and Hf isotopic compositions of detrital zircons from the paragneisses of the Quanji Massif, NW China: implications for its early tectonic evolutionary history. J. Asian Earth Sci. 54–55, 110–130.

Cheng, L.N., Zhang, C., Liu, X.C., Yang, X.S., Zhou, Y.S., Horn, I., Weyer, S., Holtz, F., 2021. Significant boron isotopic fractionation in the magmatic evolution of Himalayan leucogranite recorded in multiple generations of tourmaline. Chem. Geol. 571, 120194.

Cheng, L., Zhang, C., Zhou, Y., Horn, I., Weyer, S., Holtz, F., 2022. Experiments reveal enrichment of ^{11}B in granitic melt resulting from tourmaline crystallisation. Geochem. Perspect. Let. 20, 37–42.

Chukwu, A., Obiora, S.C., 2021. Petrogenetic characterization of pegmatites and their host rocks in southern Akwanga, North-Central Basement Complex. Nigeria. J. Earth Syst. Sci. 130, 1–23.

da Costa, I.R., Mourão, C., Récio, C., Guimarães, F., Antunes, I.M., Ramos, J.F., Barriga, F.J.A.S., Milton, J.A., 2014. Tourmaline occurrences within the Penamacor-Monsanto granitic pluton and host-rocks (Central Portugal): genetic implications of crystal-chemical and isotopic features. Contrib. Mineral. Petr. 167, 1–23.

Ding, K., Seyfried, J.R.W.E., 1992. Determination of Fe-Cl complexing in the low pressure supercritical region (NaCl fluid): Iron solubility constraints on pH of subseafloor hydrothermal fluids. Geochim. Cosmochim. Ac. 56, 3681–3692.

Drivenes, K., Larsen, R.B., Müller, A., Sørensen, B.E., Wiedenbeck, M., Raanes, M.P., 2015. Late-magmatic immiscibility during batholith formation: assessment of B isotopes and trace elements in tourmaline from the Land's End granite, SW England. Contrib. Mineral. Petr. 169, 1–27.

Dutrow, B.L., Henry, D.J., 2011. Tourmaline: a geologic DVD. Elements 7, 301–306.

Guo, J., Xiang, L., Zhang, R., Yang, T., Wu, K., Sun, W., 2022. Chemical and boron isotopic variations of tourmaline deciphering magmatic-hydrothermal evolution at the Gejiu Sn-polymetallic district. South China. Chem. Geol. 593, 120698.

Hawthorne, F.C., Henry, D.J., 1999. Classification of the minerals of the tourmaline group. Eur. J. Mineral. 11, 201–215.

Henry, D.J., Guidotti, C.V., 1985. Tourmaline as a petrogenetic indicator mineral: an example from the staurolite-grade metapelites of NW Maine. Am. Mineral. 70 (1–2), 1–15.

Henry, D.J., Novák, M., Hawthorne, F.C., Ertl, A., Dutrow, B.L., Uher, P., Pezzotta, F., 2011. Nomenclature of the tourmaline-supergroup minerals. Am. Mineral. 96, 895–913.

Hervig, R.L., Moore, G.M., Williams, L.B., Peacock, S.M., Holloway, J.R., Roggensack, K., 2002. Isotopic and elemental partitioning of boron between hydrous fluid and silicate melt. Am. Mineral. 87, 769–774.

Holtz, F., Dingwell, D.B., Behrens, H., 1993. Effects of F, B_2O_3 and P_2O_5 on the solubility of water in haplogranite melts compared to natural silicate melts. Contrib. Mineral. Petr. 113, 492–501.

Huang, H., Niu, Y., Nowell, G., Zhao, Z., Yu, X., Zhu, D.C., Mo, X.X., Ding, S., 2014. Geochemical constraints on the petrogenesis of granitoids in the East Kunlun Orogenic belt, northern Tibetan Plateau: Implications for continental crust growth through syn-collisional felsic magmatism. Chem. Geol. 370, 1–18.

Hulsbosch, N., Hertogen, J., Dewaele, S., André, L., Muchez, P., 2014. Alkali metal and rare earth element evolution of rock-forming minerals from the Gatumba area pegmatites (Rwanda): Quantitative assessment of crystal-melt fractionation in the regional zonation of pegmatite groups. Geochim. Cosmochim. Ac. 132, 349–374.

Jahns, R.H., Burnham, C.W., 1969. Experimental studies of pegmatite genesis: I. A model for the derivation and crystallization of granitic pegmatites. Econ. Geol. 64, 843–864.

Jiang, S.Y., Palmer, M.R., 1998. Boron isotope systematics of tourmaline from granites and pegmatites; a synthesis. Eur. J. Mineral. 10, 1253–1265.

Jolliff, B.L., Papike, J.J., Shearer, C.K., 1986. Tourmaline as a recorder of pegmatite evolution; Bob Ingersoll pegmatite, Black Hills, South Dakota. Am. Mineral. 71, 472–500.

Li, J.X., Fan, W.M., Zhang, L.Y., Ding, L., Yue, Y.H., Xie, J., Cai, F.L., Sein, K., 2020. B-rich melt immiscibility in Late Cretaceous Nattaung granite, Myanmar: implication by composition and B isotope in tourmaline. Lithos 356, 105380.

Li, X.C., Niu, M.L., Yakymchuk, C., Yan, Z., Fu, C.L., Zhao, Q.Q., 2018. Anatexis of former arc magmatic rocks during oceanic subduction: a case study from the north Wulan gneiss complex. Gondw. Res. 61, 128–149.

Li, J.K., Zou, T.R., Liu, X.F., Wang, D.H., Ding, X., 2015. The metallogenetic regularities of lithium deposits in China. Acta Geol. Sin-Engl. 89, 652–670.

Liu, C.X., Sun, F.Y., Qian, Y., Wu, D.Q., Hui, C., Lu, Y.H., 2021. Vertical zonation characteristics of Chakabeishan Li-Be rare-metal pegmatite deposit in northern margin of Qaidam Basin, Qinghai Province. Global Geol. 40, 843–880. in Chinese with English abstract.

Liu, C.X., Sun, F.Y., Li, J.Q., Han, J., Qian, Y., Zhang, Y.J., Hui, C., Bakht, S., 2022a. The Petrogenesis and Metallogenesis of the Chakabeishan Li-Be Pegmatitic Deposit in Qinghai, NW China: Evidence from Geochronology, Geochemistry, and Mineral Geochemistry. Ore Geol. Rev. 150, 105186.

Liu, J.H., Wang, Q., Xu, C.B., Zhou, J.S., Wang, B.Z., Li, W.F., Li, S.P., Huang, T.Y., Yan, Q.H., Song, T.Z., Wang, C.T., Zheng, Y., Wang, J.S., 2022b. Geochronology of the Chakabeishan Li-(Be) rare-element pegmatite, Zongwulong orogenic belt, northwest China: Constraints from columbite-tantalite U-Pb and muscovite-lepidolite 40Ar/39Ar dating. Ore Geol. Rev. 146, 104930.

Liu, J.H., Wang, Q., Wang, B.Z., Li, W.F., Xu, C.B., Li, S.P., Wang, Z.L., Hao, L.L., Song, T.Z., Wang, C.T., Zheng, Y., Wang, J.S., 2023. Petrogenesis of the Chakabeishan pegmatites, North Qaidam Terrane: Implications for Indosinian lithium mineralization in the northern Tibetan Plateau. Lithos 440–441, 107025.

London, D., 2011. Experimental synthesis and stability of tourmaline: a historical overview. Can. Mineral. 49, 117–136.

London, D., 2015. Reply to Thomas and Davidson on" A petrologic assessment of internal zonation in granitic pegmatites"(London, 2014a). Lithos 212, 469–484.

London, D., 2018. Ore-forming processes within granitic pegmatites. Ore Geol. Rev. 101, 349–383.

London, D., Manning, D.A., 1995. Chemical variation and significance of tourmaline from southwest England. Econ. Geol. 90, 495–519.

London, D., Hunt, L.E., Schwing, C.R., Guttery, B.M., 2020. Feldspar thermometry in pegmatites: truth and consequences. Contrib. Mineral. Petr. 175, 1–21.

Lv, Z.H., Zhang, H., Tang, Y., 2021. Anatexis origin of rare metal/earth pegmatite: evidences from the Permian pegamtites in the Chinese Altai. Lithos 380, 105865.

Maner IV, J.L., London, D., 2018. Fractionation of the isotopes of boron between granitic melt and aqueous solution at 700 C and 800 C (200 MPa). Chem. Geol. 489, 16–27.

McNeil, A.G., Linnen, R.L., Flemming, R.L., Fayek, M., 2020. An experimental approach to examine fluid-melt interaction and mineralization in rare-metal pegmatites. Am. Mineral. 105, 1078–1087.

Meyer, C., Wunder, B., Meixner, A., Romer, R.L., Heinrich, W., 2008. Boron-isotope fractionation between tourmaline and fluid: an experimental re-investigation. Contrib. Mineral. Petr. 156, 259–267.

Müller, A., Ihlen, P.M., Snook, B., Larsen, R.B., Flem, B., Bingen, B., Williamson, B.J., 2015. The chemistry of quartz in granitic pegmatites of southern Norway: Petrogenetic and economic implications. Econ. Geol. 110, 1737–1757.

Orlando, A., Ruggieri, G., Chiarantini, L., Montegrossi, G., Rimondi, V., 2017. Experimental investigation of biotite-rich schist reacting with B-bearing fluids at upper crustal conditions and correlated tourmaline formation. Minerals 7, 155–178.

Palmer, M.R., Swihart, G.H., 1996. Boron isotope geochemistry: an overview. In: Grew, E.S., Anovitz, L.M. (Eds.), Boron: Mineralogy, Petrology and Geochemistry, Reviews in Mineralogy, vol. 33. Berlin, Boston, pp. 709-744.

Palmer, M.R., London, D., Morgan VI, G.B., Babb, H.A., 1992. Experimental determination of fractionation of $^{11}B/^{10}B$ between tourmaline and aqueous vapor: a temperature and pressure-dependent isotopic system. Chem. Geol. 101: 123-129.

Pan, T., Ding, Q.F., Zhou, X., Li, S.P., Han, J., Cheng, L., 2021. Columbite-tantalite group mineral U-Pb geochronology of Chaqiabeishan Li-rich granitic pegmatites in the Quanji Massif, NW China: Implications for the Genesis and Emplacement Ages of Pegmatites. Front. in Earth Sci. 8, 606951.

Pichavant, M., 1981. An experimental study of the effect of boron on a water saturated haplogranite at 1 kbar vapour pressure. Contrib. Mineral. Petr. 76, 430–439.

Qiu, K.F., Yu, H.C., Hetherington, C., Huang, Y.Q., Yang, T., Deng, J., 2021. Tourmaline composition and boron isotope signature as a tracer of magmatic-hydrothermal processes. Am. Mineral. 106, 1033–1044.

Raschke, M.B., Stern, C.R., Anderson, E.J., Alexandra Skewes, M., Lang Farmer, G., Allaz, J.M., Persson, P.M., 2021. Bulk composition of a zoned rare-earth minerals-bearing pegmatite in the Pikes Peak granite batholith near Wellington Lake, central Colorado, USA. Rocky Mt Geol. 56, 1–18.

Ren, Y.F., Chen, D.L., Wang, H.J., Zhu, X.H., Bai, B.W., 2021. Grenvillian and early paleozoic polyphase metamorphism recorded by eclogite and host garnet mica schist in the north Qaidam Orogenic belt. Geosci. Front. 6, 101170.

Ribacki, E., Trumbull, R.B., López de Luchi, M.G., Altenberger, U., 2022. The Chemical and B-Isotope Composition of Tourmaline from Intra-Granitic Pegmatites in the Las Chacras-Potrerillos Batholith. Argentina. Can. Mineral. 60, 49–66.

Schmidt, C., Thomas, R., Heinrich, W., 2005. Boron speciation in aqueous fluids at 22 to 600 °C and 0.1 MPa to 2 GPa. Geochim. Cosmochim. Ac. 69, 275–281.

Shao, F., Niu, Y., Liu, Y., Chen, S., Kong, J., Duan, M., 2017. Petrogenesis of Triassic granitoids in the East Kunlun Orogenic Belt, northern Tibetan Plateau and their tectonic implications. Lithos 282, 33–44.

Siani, M.G., Mehrabi, B., Bayat, S., Neubauer, F., Cao, S., 2021. Geochronology, geochemistry and mineral chemistry of Malayer-Boroujerd-Shazand pegmatite dikes, Sanandaj-Sirjan zone. NW Iran. Int. J. Earth Sci. 110, 1139–1167.

Siegel, K., Wagner, T., Trumbull, R.B., Jonsson, E., Matalin, G., Wälle, M., Heinrich, C. A., 2016. Stable isotope (B, H, O) and mineral-chemistry constraints on the magmatic to hydrothermal evolution of the Varuträsk rare-element pegmatite (Northern Sweden). Chem. Geol. 421, 1–16.

Slack, J.F., Trumbull, R.B., 2011. Tourmaline as a recorder of ore-forming processes. Elements 7, 321–326.

Smith, M.P., Yardley, B.W.D., 1996. The boron isotopic composition of tourmaline as a guide to fluid processes in the southwestern England orefield: an ion microprobe study. Geochim. Cosmochim. Ac. 60, 1415–1427.

Song, S.G., Niu, Y., Su, L., Zhang, C., Zhang, L.F., 2014. Continental orogenesis from ocean subduction, continent collision/subduction, to orogen collapse, and orogen recycling: the example of the North Qaidam UHPM belt, NW China. Earth Sci. Rev. 129, 59–84.

Sun, W.L., Ma, Y., Song, Q.W., 2021. Characteristics and research progress of granitic pegmatite type Lithium deposit in China. Geol. Explor. 57, 478–496 (in Chinese with English abstract).

Sun, W.L., Liu, Y., Zhang, Z.W., 2022. Research progress on petrogenesis of LCT-type granitic pegmatite and therein lithium enrichment mechanism. Northwest. Geol. 55, 35–55 (in Chinese with English abstract).

Sun, W.L., Zhao, Z.D., Mo, X.X., Wei, C.J., Dong, G.C., Li, X.W., Yuan, W.M., Wang, T., Yang, S., Wang, B.Z., Pan, T., Han, J., Cao, H.L., Tamg, Y., Zhang, L.L., 2023. Age and composition of columbite-tantalite group minerals in the spodumene pegmatite from the Chakabeishan deposit, Northern Tibetan Plateau and their implications. Minerals 13 (2), 201.

Thomas, R., Davidson, P., 2015. Comment on "A petrologic assessment of internal zonation in granitic pegmatites" by David London (2014). Lithos 212, 462–468.

Tonarini, S., Forte, C., Petrini, R., Ferrara, G., 2003. Melt/biotite $^{11}B/^{10}B$ isotopic fractionation and the boron local environment in the structure of volcanic glasses. Geochim. Cosmochim. Ac. 67, 1863–1873.

Troch, J., Huber, C., Bachmann, O., 2022. The physical and chemical evolution of magmatic fluids in near-solidus silicic magma reservoirs: Implications for the formation of pegmatites. Am. Mineral. 107, 190–205.

Trumbull, R.B., Chaussidon, M., 1999. Chemical and boron isotopic composition of magmatic and hydrothermal tourmalines from the Sinceni granite-pegmatite system in Swaziland. Chem. Geol. 153, 125–137.

Trumbull, R.B., Krienitz, M.S., Gottesmann, B., Wiedenbeck, M., 2008. Chemical and boron-isotope variations in tourmalines from an S-type granite and its source rocks: the Erongo granite and tourmalinites in the Damara Belt. Namibia. Miner. Petrol. 155, 1–18.

Trumbull, R.B., Beurlen, H., Wiedenbeck, M., Soares, D.R., 2013. The diversity of B-isotope variations in tourmaline from rare-element pegmatites in the Borborema Province of Brazil. Chem. Geol. 352, 47–62.

Trumbull, R.B., Slack, J.F., 2018. Boron isotopes in the continental crust: granites, pegmatites, felsic volcanic rocks, and related ore deposits. In: Marschall, H., Foster, G. (Eds.), Boron Isotopes: The Fifth Element. Springer International Publishing, Cham, pp. 249–272.

van Hinsberg, V.J., Henry, D.J., Marschall, H.R., 2011. Tourmaline: an ideal indicator of its host environment. Can. Mineral. 49, 1–16.

Wang, D.H., Dai, H.Z., Liu, S.B., Wang, C.H., Yu, Y., Dai, J.J., Liu, L.J., Yang, Y.Q., Ma, S.C., 2020b. Research and exploration progress on lithium deposits in China. China Geol. 1, 137–152.

Wang, B.Z., Han, J., Xie, X.L., Chen, J., Wang, T., Xue, W.W., Bai, Z.H., Li, S.P., 2020a. Discovery of the Indosinian (Beryl-bearing) spodumene pegmatitic dike swarm in the Chakaibeishan area in the northeastern margin of the Tibetan plateau: implications for Li-Be mineralization. Geotectonia et Metallogenia 44, 69–79 (in Chinese with English abstract).

Wise, M.A., Brown, C.D., 2019. Cathodoluminescence (CL) microscopy: a technique for understanding the dynamics of pegmatite crystallization. Can. Mineral. 57, 821–823.

Wu, C.L., Gao, Y.H., Li, Z.L., Lei, M., Qin, H.P., Li, M.Z., Liu, C.H., Ronald, B.F., Paul, T.R., Joseph, L.W., 2014. Zircon SHRIMP U-Pb dating of granites from Dulan and the chronological framework of the North Qaidam UHP belt. NW China. Sci. China-Earth Sci. 57, 2945–2965.

Wunder, B., Meixner, A., Romer, R.L., Wirth, R., Heinrich, W., 2005. The geochemical cycle of boron: constraints from boron isotope partitioning experiments between mica and fluid. Lithos 84, 206–216.

Xiao, J., Xiao, Y.K., Jin, Z.D., He, M.Y., Liu, C.Q., 2013. Boron isotope variations and its geochemical application in nature. Aust. J. Earth. Sci. 60, 431–447.

Xing, C.M., Wang, C.Y., Wang, H., 2020. Magmatic-hydrothermal processes recorded by muscovite and columbite-group minerals from the Bailongshan rare-element pegmatites in the West Kunlun-Karakorum orogenic belt. NW China. Lithos 364, 105507.

Xu, J., Zhang, G.B., Li, N., Lin, M., Wang, J.X., 2020. In situ boron isotope analysis method for tourmaline and muscovite by LA-MC-ICP MS and its applications. Acta Petrol. Mineral. 39, 323–334 (in Chinese with English abstract).

Yan, Q., Li, J., Li, X., Liu, Y., Xiong, X., 2020. Source of the Zhawulong granitic pegmatite-type lithium deposit in the Songpan-Ganzê Orogenic belt, western Sichuan, China: constrants from Sr-Nd-Hf isotopes and petrochemistry. Lithos 3, 378–379.

Yan, Q.H., Wang, H., Chi, G., Wang, Q., Hu, H., Zhou, K., Zhang, X.Y., 2022. Recognition of a 600km long late Triassic rare metal (Li-Rb-Be-Nb-Ta) pegmatite belt in the western Kunlun Orogenic Belt, western China. Econ. Geol. 117, 213–236.

Yu, S.Y., Li, S.Z., Zhang, J.X., Peng, Y.B., Somerville, I., Liu, Y.J., Wang, Z.Y., Li, Z.F., Yao, Y., Li, Y., 2019. Multistage anatexis during tectonic evolution from oceanic subduction to continental collision: a review of the North Qaidam UHP Belt, NW China. Earth Sci. Rev. 191, 190–211.

Zhang, B., Qi, F.Y., Gao, X.Z., Li, X.L., Shang, Y.T., Kong, Z.Y., Jia, L.Q., Meng, J., Guo, H., Fang, F.K., Liu, Y.B., Jiang, X., Chai, H., Liu, Z., Ye, X.T., Wang, G.D., 2022. China Geol. 5, 734–767.

Zhang, L., Wang, Q.Y., Chen, N.S., Sun, M., Santosh, M., Ba, J., 2014. Geochemistry and detrital zircon U-Pb and Hf isotopes of the paragneiss suite from the Quanji Massif. SE Tarim Craton: implication for Paleoproterozoic tectonics in NW China. J. Asian Earth Sci. 95, 33–50.

Zhao, H., Chen, B., Huang, C., Bao, C., Yang, Q., Cao, R., 2022. Geochemical and Sr-Nd-Li isotopic constraints on the genesis of the Jiajiaka Li-rich pegmatites, eastern Tibetan Plateau: implications for Li mineralization. Contrib. to Mineral. Petrol. 177 (1), 1–16.

Zhao, H.D., Zhao, K.D., Palmer, M.R., Jiang, S.Y., 2019. In-situ elemental and boron isotopic variations of tourmaline from the Sanfang granite, South China: Insights into magmatic-hydrothermal evolution. Chem. Geol. 504, 190–204.

Zhao, H.D., Zhao, K.D., Palmer, M.R., Jiang, S.Y., Chen, W., 2021. Magmatic-hydrothermal mineralization processes at the Yidong tin deposit, south China: insights from in situ chemical and boron Isotope changes of tourmaline. Econ. Geol. 116, 1625–1647.

Zhou, Q., Li, W.C., Wang, G.C., Liu, Z., Lai, Y., Huang, J.H., Yan, G.Q., Zhang, Q.C., 2019. Chemical and boron isotopic composition of tourmaline from the Conadong leucogranite-pegmatite system in South Tibet. Lithos 326-327, 529–539.

Zhou, Q., Qin, K., Tang, D., Wang, C., 2022. A Combined EMPA and LA-ICP-MS Study of Muscovite from Pegmatites in the Chinese Altai, NW China: Implications for Tracing Rare-Element Mineralization Type and Ore-Forming Process. Minerals 12, 377–400.